J|A|C|S ARTICLES

Published on Web 05/26/2009

Molecule-Like Eu^{3+}-Dimers Embedded in an Extended System Exhibit Unique Photoluminescence Properties

Duarte Ananias,[†] Mariya Kostova,[†] Filipe A. A. Paz,[†] Albano N. C. Neto,[‡] Renaldo T. De Moura, Jr.,[‡] Oscar L. Malta,[‡] Luis D. Carlos,*[,†] and João Rocha*[,†]

Departments of Chemistry and Physics, CICECO, University of Aveiro, 3810-193 Aveiro, Portugal, and Departamento de Química Fundamental, CCEN-UFPE, Recife-PE, 50670-901, Brazil

Received March 9, 2009; E-mail: lcarlos@ua.pt; rocha@ua.pt

Abstract: Much is known about the photoluminescence of lanthanide-containing systems, particularly amorphous silicates or organic−inorganic hybrids and crystalline metal−organic frameworks. Comparatively, stoichiometric microporous Ln-silicates are poorly studied. Here, we report the exceptional photoluminescence of microporous AV-24, $K_7[Ln_3Si_{12}O_{32}]\cdot xH_2O$ (Ln^{3+} = Sm^{3+}, Eu^{3+}, Gd^{3+}, Tb^{3+}), the first silicate possessing $Ln^{3+}-O-Ln^{3+}$ dimers (inter-Ln distance *ca.* 3.9 Å), i.e., two edge-sharing $\{LnO_6\}$ octahedra embedded in a crystalline matrix. It is totally unprecedented that in AV-24 $Eu^{3+}-O-Eu^{3+}$ dimers behave like discrete entities, i.e., molecules: they (i) have a unique emission signature, with pseudopoint group symmetry (C_i), different from the symmetry (C_1) of each individual constituent Eu^{3+} ion, and (ii) exhibit the unusually long $^5D_0$ lifetime of 10.29 ms (12 K). In accord with the experimental evidence, a molecular orbital model shows that the $Eu^{3+}-O-Eu^{3+}$ dimers are energetically more stable than the individual metal ions.

1. Introduction

Trivalent lanthanide ions (Ln^{3+}) hold a special place in photonics because of their exceptional luminescence features, especially with respect to their application in phosphors,[1] generation, and amplification of light in lasers (e.g., Nd^{3+} in yttrium aluminum garnet, YAG)[2] and optical amplifiers (e.g., Er^{3+}-doped fiber amplifiers).[3]

Due to the parity and spin-forbidden character of the 4f−4f transitions, direct Ln^{3+} photoexcitation is not very efficient (typically with absorption cross sections smaller than 4×10^{-20} cm^2), thus limiting the light output. This may be overcome, with the resultant increase (often huge) of the Ln^{3+} luminescence intensity, thermal and photochemical stability, and mechanical and processability properties, through the smart design of Ln-containing multifunctional materials, such as organic−inorganic hybrids,[4] metal−organic frameworks,[5] and microporous (stoichiometric) silicates.[6] The latter materials are reminiscent of zeolites, combining microporosity and photoluminescence, while preserving excellent thermal stability. Certain microporous lanthanide silicates display very unusual photoluminescence properties. A case in point is that of chiral $Na_3[(Y,Ln)Si_3O_9]\cdot 3H_2O$ for which it has been shown that Eu^{3+} photoluminescence spectroscopy, with excitation by unpolarized light in the absence of an external magnetic field, is able to identify enantiomeric domains.[6d] Here we wish to report on the exceptional photoluminescence properties of another microporous lanthanide silicate, known as AV-24. Essentially, these properties stem from this being the first example of an extended solid in which $Ln^{3+}-O-Ln^{3+}$ dimers are embedded in the framework and behave like a molecule.

The importance of metal dimers on the optical properties of materials has been recognized. For example, some reports are available on heterobimetallic assemblies as a new class of visible-light absorbing chromophores, such as the anchored Zr(IV)−O−Cu(I) assembly on mesoporous silica MCM-41 (ref 7 and references therein). As far as Ln-containg materials are concerned, dimers have been found in many inorganic−organic hybrids. We have used the Cambridge Structural Database (CSD, Version 5.30 November 2008 with one update) to perform a systematic search of such compounds. As expected, and largely due to the fast-growing research field of metal−organic frameworks, the vast majority of dimers arise from carboxylate *syn*,*syn*-bridges, with over 150 structures having Eu^{3+}. Remarkably, none has Ln centers in a typical octahedral geometry. For single-oxygen bridges, as those in the silicate materials reported in this paper, 119 compounds were found of which only two have Eu^{3+} in a typical octahedral coordination and sharing a polyhedron edge. Only the structure of Fleming et al. is a true dimer, though as a discrete complex, with an intermetallic distance of *ca.* 3.8 Å.[8]

[†] University of Aveiro.
[‡] CCEN-UFPE.

(1) (a) Justel, T.; Nikol, H.; Ronda, C. *Angew. Chem., Int. Ed.* **1998**, *37*, 3085–3103. (b) Werts, M. H. V. *Sci. Progress* **2005**, *88*, 101–131. (c) Bünzli, J.-C. G.; Piguet, C. *Chem. Soc. Rev.* **2005**, *34*, 1048–1077.
(2) Marling, J. *IEEE J. Sel. Top. Quant.* **1978**, *14*, 56–62.
(3) Polman, A.; van Veggel, F. C. J. M. *J. Opt. Soc. Am. B* **2004**, *21*, 871–892.
(4) (a) Comby, S.; Bünzli, J.-C. G. In *Handbook on the Physics and Chemistry of Rare Earths*; GschneidnerK. A., Jr., Bünzli, J.-C. G., Pecharsky, V. K., Eds.; Elsevier Science: New York, 2007, pp 217−254. (b) Escribano, P.; Julian-Lopez, B.; Planelles-Arago, J.; Cordoncillo, E.; Viana, B.; Sanchez, C. *J. Mater. Chem.* **2008**, *18*, 23–40. (c) Carlos, L. D.; Ferreira, R. A. S.; Bermudez, V. D.; Ribeiro, S. J. L. *Adv. Mater.* **2009**, *21*, 509–534.

 10.1021/ja901820z CCC: $40.75

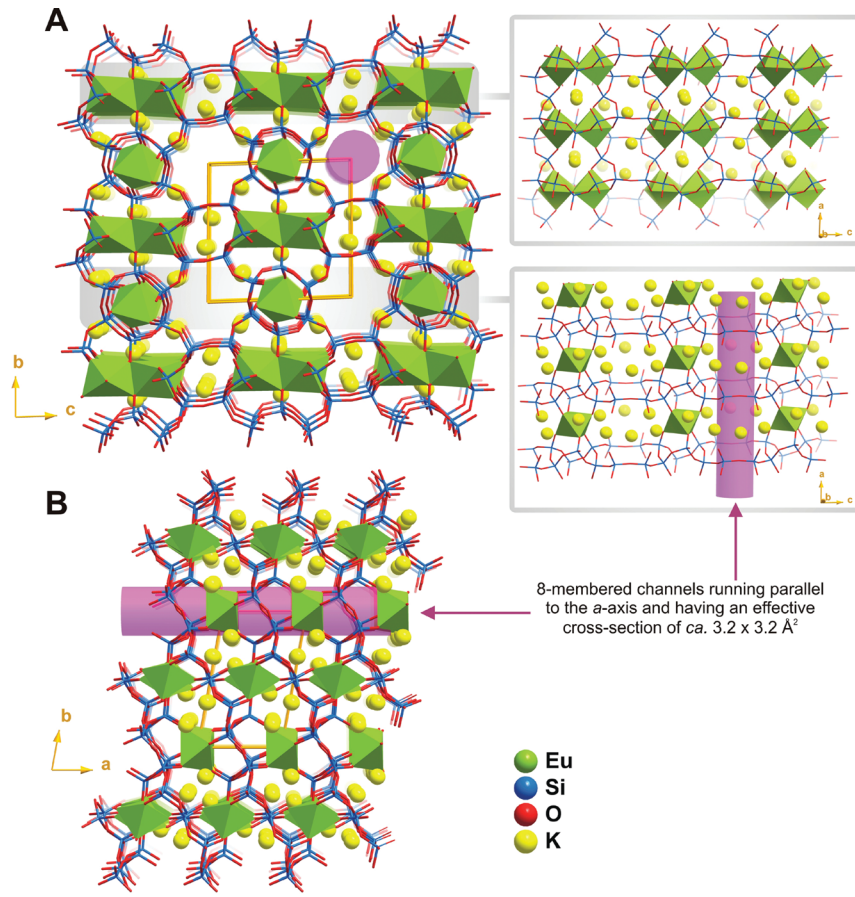

Figure 1. Crystal structure of $K_7[Eu_3Si_{12}O_{32}]\cdot 4H_2O$ viewing along the (A) [100] and (B) [001] crystallographic directions. Fragments of the framework depicting layers of isolated $\{EuO_6\}$ octahedra and centrosymmetric dimeric $\{Eu_2O_{10}\}$ units are shown on the right.

In 1981, Pushcharovskii and co-workers described $K_{8-x}[Yb_3Si_{12}O_{32}](OH)_{1-x} \cdot xH_2O$ (x *ca.* $^2/_3$),[9] while nearly 20 years later Haile et al., in a follow-up from an early study on the conductivity of rare-earth silicates,[10] reported $K_8[Nd_3Si_{12}O_{32}](OH)$, a material with a similar structure but not potassium deficient.[11] The AV-24, $K_7[Ln_3Si_{12}O_{32}]\cdot xH_2O$ (Ln^{3+} = Sm^{3+}, Eu^{3+}, Gd^{3+}, Tb^{3+}), system reported here is yet another member of this family whose structure is related to, although different from, the structures of Pushcharovskii's and Haile's materials.

2. Crystal Structure

The structure of phyllosilicate AV-24 materials (Figure 1) is built up of six crystallographic distinct $\{SiO_6\}$ tetrahedra, which polymerize in the *bc* plane of the unit cell into anionic $(Si_{12}O_{32})_n^{16n-}$ layers exhibiting a periodic alternation between two types of six-, one eight-, and a highly distorted twelve-membered rings. Layers stack in a parallel fashion along the [100] direction, leading to an alignment of all the eight-membered rings along the same direction, originating tunnels with an effective cross section of *ca.* 3.2 × 3.2 Å, housing highly disordered water molecules (Figure 1). The "glue" holding adjacent layers together consists of two crystallographically distinct lanthanide centers, Ln(1) and Ln(2), both coordinated by six individual $\{SiO_4\}$ tetrahedra, with coordination geometries resembling distorted octahedra (see further details in the Supporting Information). While Ln(1) is located at a crystallographic center of inversion (isolated octahedra in Figure 1), Ln(2) appears as centrosymmetric binuclear units (Ln-dimers in Figure 1) formed by a μ_2-bridging oxygen atom from a $\{SiO_4\}$ tetrahedron. In Eu-AV-24, the $Eu^{3+}-Eu^{3+}$ distance within this dimeric unit is 3.8742(4) Å which, to the best of our knowledge, constitutes to date the shortest distance between Eu^{3+} centers in stoichiometric lanthanide silicates. Moreover, it is also important to emphasize that the AV-24 materials constitute the first examples in which these dimeric units are embedded in a

(5) (a) Devic, T.; Serre, C.; Audebrand, N.; Marrot, J.; Férey, G. *J. Am. Chem. Soc.* **2005**, *127*, 12788–12789. (b) Guo, X.; Zhu, G. S.; Li, Z. Y.; Chen, Y.; Li, X. T.; Qiu, S. L. *Inorg. Chem.* **2006**, *45*, 4065–4070. (c) Cunha-Silva, L.; Mafra, L.; Ananias, D.; Carlos, L. D.; Rocha, J.; Paz, F. A. A. *Chem. Mater.* **2007**, *19*, 3527–3538. (d) Harbuzaru, B. V.; Corma, A.; Rey, F.; Atienzar, P.; Jorda, J. L.; Garcia, H.; Ananias, D.; Carlos, L. D.; Rocha, J. *Angew. Chem., Int. Ed.* **2008**, *47*, 1080–1083. (e) Zhu, X. D.; Lu, J.; Li, X. J.; Gao, S. Y.; Li, G. L.; Xiao, F. X.; Cao, R. *Cryst. Growth Des.* **2008**, *8*, 1897–1901.
(6) (a) Rocha, J.; Carlos, L. D. *Curr. Opin. Solid State Mater. Sci.* **2003**, *7*, 199–205. (b) Ferreira, A.; Ananias, D.; Carlos, L. D.; Morais, C. M.; Rocha, J. *J. Am. Chem. Soc.* **2003**, *125*, 14573–14579. (c) Ananias, D.; Kostova, M.; Paz, F. A. A.; Ferreira, A.; Carlos, L. D.; Klinowski, J.; Rocha, J. *J. Am. Chem. Soc.* **2004**, *126*, 10410–10417. (d) Ananias, D.; Paz, F. A. A.; Carlos, L. D.; Geraldes, C. F. G. C.; Rocha, J. *Angew. Chem., Int. Ed.* **2006**, *45*, 7938–7942. (e) Kostova, M. H.; Ferreira, R. A. S.; Ananias, D.; Carlos, L. D.; Rocha, J. *J. Phys. Chem. B* **2006**, *110*, 15312–15316. (f) Evans, R. C.; Ananias, D.; Douglas, A.; Douglas, P.; Carlos, L. D.; Rocha, J. *J. Phys. Chem. C* **2008**, *112*, 260–268.
(7) Lin, W. Y.; Frei, H. *J. Am. Chem. Soc.* **2005**, *127*, 1610–1611.
(8) Fleming, S.; Gutsche, C. D.; Harrowfield, J. M.; Ogden, M. I.; Skelton, B. W.; Stewart, D. F.; White, A. H. *Dalton Trans.* **2003**, 3319–3327.
(9) Pushcharovskii, D. I.; Dago, A. M.; Pobedimskaia, E. A.; Belov, N. V. *Dokl. Akad. Nauk SSSR* **1981**, *258*, 1111–1115.
(10) Haile, S. M.; Wuensch, B. J.; Siegrist, T.; Laudise, R. A. *Solid State Ion.* **1992**, *53−6*, 1292–1301.
(11) Haile, S. M.; Wuensch, B. J.; Siegrist, T. *J. Solid State Chem.* **1999**, *148*, 406–418.

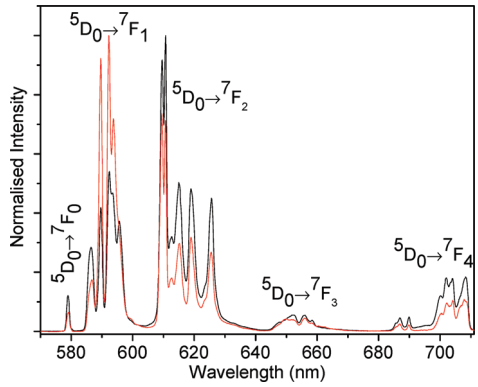

Figure 2. Emission spectra of $K_7[Eu_3Si_{12}O_{32}]\cdot 4H_2O$ at 12 K. The excitation was performed at 393 (black line) and 525.5 nm (red line).

framework matrix. Indeed, all related crystalline hybrid structures reported in the literature are discrete (0D) complexes, as revealed by a systematic search in the Cambridge Structural Database.

3. Exceptional Photoluminescence Properties

The excitation spectra, measured at room temperature and 12 K, of $K_7[Eu_3Si_{12}O_{32}]\cdot 4H_2O$ and $K_7[(Gd_{2.7}Eu_{0.3})Si_{12}O_{32}]\cdot 4H_2O$ (Eu,Gd-AV-24), monitored at the $^5D_0 \rightarrow {}^7F_2$ transition, 610.5 nm (Figures S5 and S6, Supporting Information), display a series of sharp lines assigned to the $^7F_{0,1} \rightarrow {}^5D_{0-4}$, $^5{}^L G_6$, $^5G_{2-6}$, $^5H_{3-7}$, and $^5F_{1-5}$ intra $4f^6$ transitions. A faint broad band at 245 nm is ascribed to the low-spin interconfigurational $4f^6 \rightarrow 4f^5 5d^1$ transition.[12] At 12 K a second broad band is observed at 265 nm and is attributed to the $O \rightarrow Eu^{3+}$ charge-transfer (CT) transition.[6d]

The maximum absolute emission-quantum yields, measured at room temperature for an excitation at 393.5 nm, are 0.36, 0.11, and 0.10, respectively, for the pure Eu-AV-24 and Eu,Gd-AV-24 with 20% and 10% of Eu^{3+} (see below).

The emission spectra, measured at room temperature and 12 K, of Eu-AV-24 and mixed Eu,Gd-AV-24 (Figure 2 and Figures S7 and S8 in the Supporting Information) show sharp emission lines, assigned to transitions between the first excited nondegenerate $^5D_0$ state and the $^7F_{0-4}$ levels of the fundamental Eu^{3+} septet. The ligand field splits the $^5D_0 \rightarrow {}^7F_1$ and $^5D_0 \rightarrow {}^7F_2$ transitions into more than, respectively, three and five Stark components, indicating the presence of two distinct Eu^{3+} environments. The changes detected in the relative transition intensities between the Stark levels as the excitation wavelength varies from 393 ($^5{}^L G_6$) to 525.5 nm ($^5D_1$) confirm the presence of two local Eu^{3+} environments (Figure 2), in agreement with the single-crystal XRD data. These emission spectra are not compatible with the existence of a center of inversion in the structure (the isolated Eu(1) species). In the case of excitation at 393 nm (the $^7F_0 \rightarrow {}^5L_6$ transition), since $\Delta J = 6$, this transition and the subsequent $^5D_0 \rightarrow {}^7F_J$ ($J = 2-6$) emission lines would be forbidden by the usual selection rules for the Eu(1) species in a center of inversion. In other words, the well-known Ω_λ ($\lambda = 2$, 4, and 6) intensity parameters would vanish. In this case, the emission spectrum should exhibit Stark components associated only with the Eu(2) ions, and this is not observed (Figure 2). For excitation at 525.5 nm ($^7F_0 \rightarrow {}^5D_1$ transition), $\Delta J = 1$ and the transition is allowed by the magnetic dipole mechanism.

(12) van Pieterson, L.; Reid, M. F.; Wegh, R. T.; Soverna, S.; Meijerink, A. *Phys. Rev. B* **2002**, *65*, 045113.

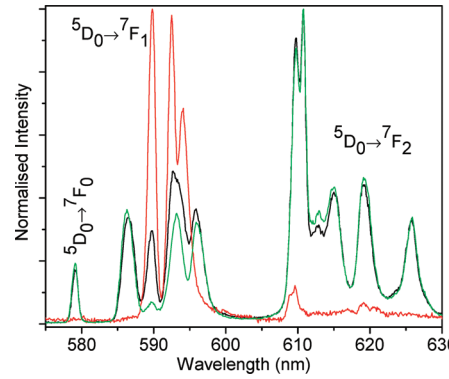

Figure 3. Time-resolved emission spectra of $K_7[Eu_3Si_{12}O_{32}]\cdot 4H_2O$ at 12 K. (Black line) Initial delay of 0.05 ms and a sample windows of 10 ms; (red line) initial delay of 25 ms and a sample windows of 10 ms; (green line) initial delay of 0.05 ms and a sample window of 0.5 ms. The excitation was fixed at 393 nm.

The emission spectrum should present Stark components corresponding to the two sites as it is indeed observed (Figure 2).

To rationalize these apparently contradictory results (single-crystal XRD and photoluminescence data) we considered a slight deviation (distortion) from the center of inversion (compatible with the ORTEP diagram ellipsoids) by considering, in a reference system of spherical coordinates centered at the Eu(1) ion, variations in angles (θ and ϕ) of less than 8%. The calculated nonvanishing Ω_λ ($\lambda = 2$ and 4) intensity parameters were of the same order of magnitude of the experimental ones ($\sim 10^{-20}$ cm^2, Table S5 in the Supporting Information).

These local environments were further investigated by time-resolved spectroscopy. By increasing the delay time and the sample window (Figure 3 and Figure S9 in the Supporting Information), the relative intensity of the $^5D_0 \rightarrow {}^7F_{0,2}$ lines decreases, while the intensities of the $^5D_0 \rightarrow {}^7F_1$ lines at 589.8, 592.4, and 594.0 nm increase. The spectrum recorded with the longest delay time (25 ms) is dominated by the magnetic-dipole $^5D_0 \rightarrow {}^7F_1$ transition, exhibiting these three Stark components, which is typical of a single Eu^{3+} local environment with a center of inversion. Moreover decreasing the sample window (for the minimum initial delay) the $^5D_0 \rightarrow {}^7F_1$ lines ascribed to this Eu^{3+} local environment are partially suppressed. On the basis of the above discussion on the local environment of the Eu(1) and Eu(2) ions, this is a rather surprising result since neither of these ions could generate these spectra.

It is possible to explain this apparent incongruity by assuming that the Eu(2) pair of ions in the dimer behave as a single entity: a molecular-like system, with a point symmetry group having a center of inversion (C_i). In fact this is corroborated by the X-ray diffraction data: each Eu(2) ion is just about the mirror image of its twin Eu(2). As for the isolated Eu(1) ion, slight distortions might also occur allowing the $^5D_0 \rightarrow {}^7F_{0,2}$ transitions. These distortions, however, are expected to be smaller than in the case of the isolated ion, since in the dimeric form the distortion effects in the two monomers tend to cancel each other. These dimers are present even at relatively low Eu^{3+} contents (e.g., in $K_7[(Gd_{2.85}Eu_{0.15})Si_{12}O_{32}]\cdot 4H_2O$, Figure S10 in the Supporting Information). The centrosymmetric Eu(2)−Eu(2) dimer explains the high relative intensity of the $^5D_0 \rightarrow {}^7F_1$ transition for excitation at 525.5 nm (the $^7F_0 \rightarrow {}^5D_1$ transition; see Figure 2), since, in this case, both species (dimers and isolated Eu^{3+} ions) may absorb, subsequently populating the

emitting $^5D_0$ level. To our knowledge, these results are the first spectroscopic evidence of symmetry effects due to the formation of a metal−metal dimer behaving as a real molecular-like system.

We now study the energy transfer among Eu^{3+} ions. The $^5D_0$ decay curve of the isolated Eu(1) ions in $K_7[(Gd_{2.7}Eu_{0.3})Si_{12}O_{32}]\cdot 4H_2O$, detected at 609 and 610.8 nm ($^5D_0 \rightarrow {}^7F_2$ transition) and measured at 12 K, is described by a single-exponential function, yielding a lifetime of 2.73 ± 0.01 ms (Figure S11a, Supporting Information). For detection at 589.6 nm (first $^5D_0 \rightarrow {}^7F_1$ line of the Eu(2)−Eu(2) dimer) the $^5D_0$ decay curve of $K_7[Eu_3Si_{12}O_{32}]\cdot 4H_2O$, detected and measured at 12 K, is characterized by a risetime of 1.89 ± 0.04 ms and a lifetime of 10.29 ± 0.04 ms, (Figure S12 and eq S6 in the Supporting Information). The risetime is of the same order of magnitude as the Eu(1) lifetime, a clear indication of a nonradiative energy-transfer process from the isolated Eu(1) ions to the Eu(2)−Eu(2) dimers, although the transfer rate is expected to be rather small due to the large donor−acceptor distance (*ca.* 6.1 Å). A lifetime of 10.29 ± 0.04 ms is one of the longest so far reported. Other examples of materials exhibiting such long lifetimes include Cs_2NaYCl_6:Eu (11.1 ms), CaF_2:Eu (11.8 ms), SrF_2:Eu (14.4 ms), BaF_2:Eu (14.6 ms) (ref 13 and references therein), and $NaCs_2[Eu(NO_2)_6]$ (10.9 ms).[14] For the diluted samples $K_7[(Gd_{3-x}Eu_x)Si_{12}O_{32}]\cdot 4H_2O$ ($x = 0.6$ and 0.3, respectively), the risetime is much shorter than that of the pure Eu sample and it decreases with decreasing Eu content (Figure S13, Supporting Information). Therefore, the decay curves were fitted with a monoexponential function, for times above 4 ms, yielding lifetimes of 11.10 ± 0.05 and 9.53 ± 0.05 ms, respectively, for 20% and 10% Eu^{3+}. Thus, the lifetime increases from the pure Eu sample to the 20% Eu sample, probably due to concentration quenching, and then it decreases for the 10% Eu sample. For the latter, we speculate that, upon Eu dilution, it becomes less and less likely to find Eu(2)−Eu(2) dimers, because there will be many Eu(2)−Gd(2) pairs, with Eu(1), rather than Gd(1), centers close by, affecting the energy transfer between Eu(1) ions and the Eu(2)−Eu(2) dimers. This reasoning may also explain the variation of the quantum yield with Eu dilution in the samples.

Above 12 K, the $^5D_0$ decay curves of the isolated Eu(1) are not monoexponential and no risetime is observed. The nonexponential character is more pronounced at higher temperatures (50−300 K; Figure S11b, Supporting Information). For a delay time as long as 25 ms (much larger than the Eu(1) $^5D_0$ lifetime in the absence of energy transfer processes; Table S4, Supporting Information), the time-resolved emission spectrum of Eu-AV-24 exhibits, essentially, the fingerprint of the Eu(2)−Eu(2) dimers, as stated above. However, surprisingly, for temperatures above 50 K, the emission lines of the Eu(1) site start to appear in the time-resolved spectrum (Figure 4). This is only possible if a thermally activated energy transfer process from the Eu(2)−Eu(2) dimer to the isolated Eu(1) ion becomes operative.

Another interesting observation is that the Eu(2)−Eu(2) dimer emission lifetime decreases as the temperature increases, in the range 12−300 K (Table S4, Supporting Information). For the mixed Gd,Eu-AV-24 sample a relatively smaller temperature dependence of the $^5D_0$ lifetime (from 10.29 to 2.84 ms in Eu-AV-24, and from 9.52 to 4.09 ms in mixed Eu,Gd-AV-24 (Table S4, Supporting Information)) is observed.

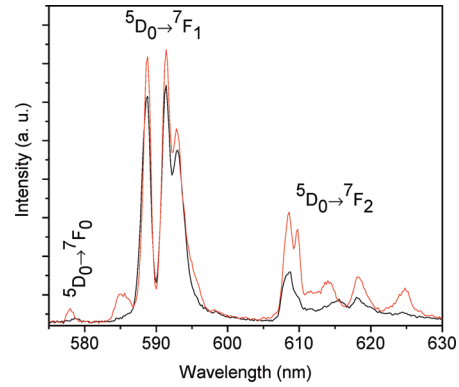

Figure 4. Time-resolved emission spectra of $K_7[Eu_3Si_{12}O_{32}]\cdot 4H_2O$ with a initial delay of 25 ms. The temperature was set at 12 K (black line) and 50 K (red line), and the excitation was fixed at 393 nm.

3.1. Experimental Intensity Parameters. The experimental intensity parameters, Ω_2 and Ω_4, were determined from the emission spectra (using the $^5D_0 \rightarrow {}^7F_2$ and $^5D_0 \rightarrow {}^7F_4$ electronic transitions, respectively) by expressing the emission intensity (I) in terms of the surface (S) under the emission curve as:

$$I_{i\rightarrow j} = \hbar w_{i\rightarrow j} A_{i\rightarrow j} N_i \equiv S_{i\rightarrow j} \qquad (1)$$

where i and j represent the initial ($^5D_0$) and final ($^7F_{0-4}$) levels, respectively, $\hbar\omega_{i\rightarrow j}$ is the transition energy, $A_{i\rightarrow j}$ corresponds to Einstein's coefficient of spontaneous emission, and N_i is the population of the $^5D_0$ emitting level. The magnetic dipole $^5D_0 \rightarrow {}^7F_1$ allowed transition was taken as reference.[15] The radiative emission rates are given by[16]

$$A_r = \frac{4e^2\omega^3}{3\hbar c^3}\chi \sum_{\lambda} \Omega_\lambda \langle {}^7F_J||U^{(\lambda)}||{}^5D_0\rangle^2 \frac{1}{2J+1} \qquad (2)$$

where $\lambda = 2$ and 4, χ is the Lorentz local-field correction term that is given by $n(n^2 + 2)^2/9$ (a refraction index $n = 1.56 \pm 0.01$ was measured), and $\langle {}^7F_J U^{(\lambda)} {}^5D_0\rangle^2$ are the squared reduced matrix elements whose values are 0.0032 and 0.0023 for $\lambda = 2$ ($J = 2$) and 4 ($J = 4$), respectively.[17] The Ω_6 parameter was not determined, since the $^5D_0 \rightarrow {}^7F_6$ transition was not observed experimentally. Therefore, we have ignored their influence on the depopulation of the $^5D_0$ excited state and, thus, the radiative contribution is estimated based only on the relative intensities of the $^5D_0 \rightarrow {}^7F_{0-4}$ transitions. Table S5 in the Supporting Information presents the values of the experimental intensity parameters, Ω_2 and Ω_4.

The theoretical approach to describe the 4f−4f intensities includes both the forced electric dipole and dynamic coupling mechanisms.[18] The theoretical intensity parameters for the isolated Eu(1) ions were calculated from the structural results, obtained from the crystallographic studies, by using the following equations:

(13) Chen, X. Y.; Liu, G. K. *J. Solid State Chem.* **2005**, *178*, 419–428.
(14) Bünzli, J.-C. G.; Petoud, S.; Moret, E. *Spectrosc. Lett.* **1999**, *32:1*, 155–163.
(15) (a) Malta, O. L.; dos Santos, M. A. C.; Thompson, L. C.; Ito, N. K. *J. Lumin.* **1996**, *69*, 77–84. (b) Malta, O. L.; Brito, H. F.; Menezes, J. F. S.; Silva, F. R. G. E.; Alves, S.; Farias, F. S.; de Andrade, A. V. M. *J. Lumin.* **1997**, *75*, 255–268.
(16) Carlos, L. D.; Messaddeq, Y.; Brito, H. F.; Ferreira, R. A. S.; Bermudez, V. D.; Ribeiro, S. J. L. *Adv. Mater.* **2000**, *12*, 594–598.
(17) Carnall, W. T.; Crosswhite, H.; Crosswhite H. M. Argonne National Laboratory, 1997.
(18) (a) Judd, B. R. *Phys. Rev.* **1962**, *127*, 750–761. (b) Ofelt, G. S. *J. Chem. Phys.* **1962**, *37*, 511–520. (c) Jørgensen, C. K.; Judd, B. R. *Mol. Phys.* **1964**, *8*, 281–290.

$$\Omega_\lambda = (2\lambda + 1)\sum_{t,p}\frac{|B_{\lambda tp}|^2}{2t+1} \quad (3)$$

with

$$B_{\lambda tp} = B^{ed}_{\lambda tp} + B^{dc}_{\lambda tp} \quad (4)$$

where

$$B^{ed}_{\lambda tp} = \theta(t,\lambda)\gamma^t_p \quad (5)$$

and

$$B^{dc}_{\lambda tp} = -\left[\frac{(\lambda+1)(2\lambda+3)}{(2\lambda+1)}\right]^{1/2}\langle 4f|r^\lambda|4f\rangle(1-\sigma_\lambda)\langle f\|C^{(\lambda)}\|f\rangle\Gamma^t_p\delta_{t,\lambda+1} \quad (6)$$

The first and second terms in the rhs of eq 4 correspond to the forced electric dipole (ed) and dynamic coupling (dc) mechanisms, respectively. The quantities γ^t_p (odd-rank ligand field parameters) and Γ^t_p (term dependent on the polarizability of the ligating atom) in eqs 5 and 6 contain a sum over the ligating atoms involving a spherical harmonic of rank t ($Y_{t,p}$). The nature of the chemical environment and structural aspects in the first coordination sphere of the lanthanide ion are taken into account in this sum, which identically vanishes when the ion is precisely located at a center of inversion. In eq 5, the numerical factor $\theta(t,\lambda)$ is a function of the lanthanide ion, and in eq 6, the quantities $\langle 4f|r^\lambda|4f\rangle$, $(1-\sigma_\lambda)$, and $\langle fC^{(\lambda)}f\rangle$ are a radial integral, shielding factor, and one-electron reduced matrix element, respectively.[15a]

In the present case, we have noticed that slight distortions of the Eu(1) coordination sphere deviating from the center of inversion, compatible with the crystallographic thermal uncertainties, were sufficient to produce nonvanishing Ω_λ intensity parameters in excellent agreement with the experimental ones. Charge factors and polarizabilities for oxygen ligands are known to vary substantially in different chemical environments. Our calculations were made by assuming for the oxygens a charge factor equal to 1 and polarizability equal to 3 Å^3, which are fairly reliable values. The results are given in Table S5, Supporting Information.

4. Rationalizing the Photoluminescence Properties: A Model for the Molecular Like Dimer

A simple molecular orbital (MO) modeling of the Eu−Eu dimer provides a reliable description of the main photoluminescence features, particularly those observed in the spectral region of the $^5D_0 \rightarrow {}^7F_0$ transition, which is ideal for probing the chemical environment of the Eu^{3+} ion. This nondegenerate transition ($J = J' = 0$) is allowed by symmetry in the point groups C_s, C_n ($n = 1-6$), and C_{mv} ($m = 2-6$),[19] and it originates from the J-mixing produced by the even components of the ligand field, particularly the mixing between the $|^7F_0\rangle$ and $|^7F_2\rangle$ levels.[20] In the following, both Eu^{3+} units in the dimer are considered to be "dressed" by the local ligand field, such that their zeroth-order energies contain the contributions from the spherical and nonspherical components of the ligand field Hamiltonian. To begin with, we consider the Hamiltonian, H, for the two Eu^{3+} ions, Eu(a) and Eu(b), separated by a distance R.

$$H = H_a + H_b + H_{ab} \quad (7)$$

The schematic MO diagram (Figure 5) represents the Eu−Eu dimer. The eigenstates $|f\rangle$ and $|f'\rangle$ correspond to the $^7F_0$ and $^5D_0$ levels, respectively. The solutions of the secular equations for both pairs of levels are of the type

$$E_+ = \frac{\alpha+\beta}{1+S_{4f}} \quad (8)$$

and

$$E_- = \frac{\alpha-\beta}{1-S_{4f}} \quad (9)$$

where

$$\alpha = E_0 + \frac{9e^2}{R} \quad (10)$$

and

$$\beta = \left(2E_0 + \frac{9e^2}{R}\right)S_{4f} \quad (11)$$

The corresponding eigenstates are given by

$$|\varphi_+\rangle = \frac{1}{\sqrt{2(1+S_{4f})}}(|f_a\rangle + |f_b\rangle) \quad (12)$$

and

$$|\varphi_-\rangle = \frac{1}{\sqrt{2(1-S_{4f})}}(|f_a\rangle - |f_b\rangle) \quad (13)$$

Analogous expressions are obtained for the excited $^5D_0$ level.

Using the so-called Wolfsberg−Helmholz approximation,[21] for the nondiagonal matrix element in eq 11, one obtains

$$\beta \cong 2E_0S_{4f} \quad (14)$$

For our purposes, it will be assumed that S_{4f} contains only the radial part of the small overlap integral between the two 4f subshells.

Since $S_{4f} \ll 1$, according to eqs 12 and 13 the relevant transition moments are by far those of the transitions between the bonding ($|\varphi'_+\rangle \rightarrow |\varphi_+\rangle$) and between the antibonding ($|\varphi'_-\rangle \rightarrow |\varphi_-\rangle$) states indicated in Figure 5, with energies, respectively, given by

$$\Delta E_+ = \Delta E_0(1+2S_{4f}) \quad (15)$$

and

$$\Delta E_- = \Delta E_0(1-2S_{4f}) \quad (16)$$

where $\Delta E_0 = E'_0 - E_0$. These two transitions are then separated by an energy difference equal to

$$\Delta E_+ - \Delta E_- = 4\Delta E_0 S_{4f} \quad (17)$$

Figure 6 shows an expansion of the time-resolved emission spectra in the region of the $^5D_0 \rightarrow {}^7F_0$ transition for $K_7[Eu_3Si_{12}O_{32}]\cdot 4H_2O$ (pure Eu^{3+}) and $K_7[(Gd_{2.4}Eu_{0.6})Si_{12}O_{32}]\cdot 4H_2O$ (mixed Eu−Gd) samples. For the pure Eu^{3+} sample, with

(19) Carlos, L. D.; Videira, A. L. L. *Phys. Rev. B* **1994**, *49*, 11721–11728.
(20) Malta, O. L. *Mol. Phys.* **1981**, *42*, 65–72.
(21) Wolfsberg, M.; Helmholz, L. *J. Chem. Phys.* **1952**, *20*, 837–843.

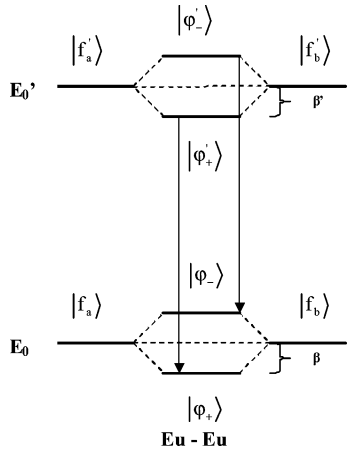

Figure 5. MO diagram of the $Eu^{3+}-O-Eu^{3+}$ dimer.

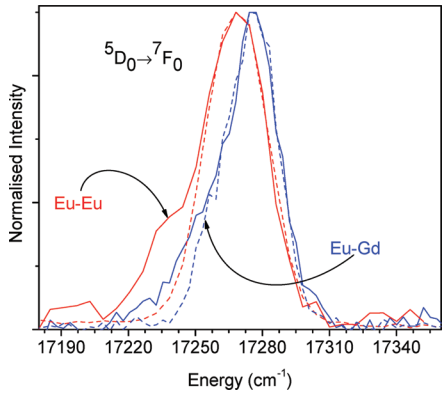

Figure 6. Time-resolved emission spectra expanded in the 5D0→7F0 region measured at 12 K. Red lines for $K_7[Eu_3Si_{12}O_{32}]\cdot 4H_2O$ with the excitation fixed at 393 nm and an initial delay of 0.05 and 25 ms for dashed and solid lines, respectively; Blue lines for $K_7[(Gd_{2.4}Eu_{0.6})Si_{12}O_{32}]\cdot 4H_2O$ with an initial delay of 0.05 ms and the excitation selected at 393 and 312 nm for dashed and solid lines, respectively. The slit emission windows are 0.2 for the pure Eu^{3+} sample and 0.1 mm for the mixed Eu−Gd sample.

an initial delay of 25 ms, a shoulder is clearly present at the lower energy side (17 238.4 ± 1.5 cm^{-1}) separated by *ca.* 30 cm^{-1} relatively to the peak at 17 268.2 ± 1.5 cm^{-1} visible on the spectrum with an initial delay of 0.05 ms ascribed to the isolated Eu^{3+} ions (Figure 5).

The $^5D_0 \rightarrow {}^7F_0$ transition of the mixed Eu−Gd sample containing 20% of Eu^{3+} and 80% of Gd^{3+}, with a delay of 0.05 ms, is also presented (see Figure 6). In this case, Eu−Eu dimeric units are much less likely to occur than Eu−Gd pairs. The observed transition has contributions from the isolated europium ions and those from the Eu−Gd pairs, where the center of inversion of the pair is no longer present. Careful examination of the profile of this transition reveals a significant broadening toward the lower energy side, which increases for the excitation on the Gd^{3+} excitation lines (e.g., 312 nm) due to energy transfer from Gd^{3+} to Eu^{3+} ions (Figure 6). This behavior is interpreted as follows. The peak at 17 275.6 ± 1.5 cm^{-1} is assigned to the isolated Eu^{3+} ions (slightly blue-shifted relatively to the spectrum of the pure Eu^{3+} sample), while the broadening toward the lower energy side, centered at 17 250.3 ± 1.5 cm^{-1}, is due to the contribution from the Eu−Gd pairs. The energy of the latter transition should correspond to ΔE_0 appearing in eqs 15−17, since from the molecular orbital point of view the interaction between the Eu^{3+} and Gd^{3+} ions is much less operative due to the mismatch between the energy levels of these two ions.

In Supporting Information Figure S14, the overlap integral S_{4f} is plotted versus the distance R. The calculations were performed using Slater-type spin−orbitals in the ZINDO program.[22] Thus, for a distance $R = 3.87$ Å ($S_{4f} = 2.2 \times 10^{-4}$), as given by the crystal structure, eq 17 leads to an energy difference of *ca.* 15 cm^{-1}, in good agreement with the value obtained from the energy difference between the shoulders at 17 238.4 ± 1.5 and 17 250.3 ± 1.5 cm^{-1} (*ca.* 12 cm^{-1}).

To estimate the nondiagonal matrix element given by eq 14, we may assume that E_0 is the energy of the 4f subshell in the Eu^{3+} ion, which has been estimated to be −1.2888 au from a restricted open-shell Hartree−Fock (ROHF) calculation. This gives $\beta \approx 120$ cm^{-1}, of the order of the ligand field interaction. This value decreases very quickly as the distance R increases. Thus, for a distance as short as 4.2 Å it is totally negligible. These estimates corroborate the idea that the Eu−Eu dimer behaves as a molecular-like system.

In conclusion, microporous Eu-AV-24 (absolute emission-quantum yield of 0.52) is the first extended system where framework embedded $Eu^{3+}-O-Eu^{3+}$ dimers behave like a molecule, exhibiting a unique emission signature and one of the longest $^5D_0$ lifetimes so far observed for Eu^{3+} in solids, 10.29 ms at 12 K (due to the forbidden character of the $^5D_0 \rightarrow {}^7F_2$ transition). According to a simple molecular orbital model (and experimental evidence), these dimers are energetically more stable than the individual metal ions, and the energy of the $^5D_0 \rightarrow {}^7F_0$ transition is *ca.* 15 cm^{-1} lower than the corresponding energy of each individual constituent Eu^{3+} ion. A complex and unusual energy transfer dynamics between the distinct Eu^{3+} ions is present. While nonradiative energy transfer from the isolated Eu(1) ions to the Eu(2)−Eu(2) dimers occurs at 12 K, at temperatures above 50 K a second, thermally activated, energy transfer process from the dimers to the isolated Eu(1) ion is in operation, for time delays larger than 25 ms.

5. Experimental Section

5.1. Sample Preparation. The syntheses of rare-earth-metal-silicates were carried out in Teflon-lined autoclaves (volume 37 cm^3, filling rate 0.62), under static hydrothermal conditions, in ovens preheated at 230 °C. All lanthanide salts were of 99.9% purity. In all the syntheses, the autoclaves were removed and quenched in cold water after an appropriate time. The obtained microcrystalline powders were filtered, washed at room temperature with distilled water, and dried at 100 °C.

5.1.1. Typical $K_7[Eu_3Si_{12}O_{32}]\cdot 4H_2O$ Synthesis. An alkaline solution was made by mixing 1.05 g of precipitate SiO_2 (93% m/m SiO_2; Riedel-de Haën), 20.32 g of H_2O, 1.50 g of KF (Carlo ERBA), and 2.05 g of KOH (Merck). An amount of 0.59 g of $EuCl_3\cdot 6H_2O$ (Aldrich) was added to this solution, and the mixture was stirred thoroughly. The gel, with composition 1.91 K_2O/1.0 SiO_2/0.05 Eu_2O_3/69 H_2O, was autoclaved under autogenous pressure for 7 days at 230 °C.

The pure $K_7[Ln_3Si_{12}O_{32}]\cdot xH_2O$ ($Ln^{3+} = Sm^{3+}$, Eu^{3+}, Gd^{3+}, Tb^{3+}) and the mixed Gd^{3+}/Eu^{3+} or Eu^{3+}/Tb^{3+} samples were prepared by introducing the desired Ln^{3+} content in the parent gel.

Within experimental error, chemical analysis by EDS confirmed the K/Ln/Si molar ratios of *ca.* 7:3:12 given by the single-crystal XRD data. For mixed Ln^{3+} samples, no crystals rich in an individual lanthanide were found. All results indicated that lanthanides are randomly distributed within the crystals.

(22) Malta, O. L. *J. Non-Cryst. Solids* **2008**, *354*, 4770–4776.

TGA reveals a weight loss, up to 450 °C, of 3.4% and 3.3% for $K_7[Ln_3Si_{12}O_{32}]\cdot xH_2O$, ($Ln^{3+}$ = Sm^{3+} and Eu^{3+}, respectively) samples, corresponding to 3.1 and 3.0 water molecules per formula unit.

5.2. Techniques. SEM images were recorded on a Hitachi S-4100 microscope. EDS was carried out using an EDS Römteck System with a polymeric window attached to the scanning electron microscope. Thermogravimetric (TGA) curves were measured with a Mettler TG50 Thermobalance, under air at a rate of 10 °C/min.

Structure solution and refinement details from single-crystal data (and all associated references) are provided as Supporting Information.

Photoluminescence measurements were recorded on a Fluorolog-3 Model FL3-2T with a double excitation spectrometer (Triax 320), fitted with a 1200 grooves/mm grating blazed at 330 nm, and a single-emission spectrometer (Triax 320), fitted with a 1200 grooves/mm grating blazed at 500 nm, coupled to an R928P photomultiplier. The excitation sources used were a 450 W Xe arc lamp and a pulsed Xe−Hg lamp, for the steady-state and time-resolved measurements, respectively. The excitation spectra were corrected from 240 to 600 nm for the spectral distribution of the lamp intensity using a photodiode reference detector. Emission and excitation spectra were also corrected for the spectral response of the monochromators and the detector, using typical correction spectra provided by the manufacturer. The measurements at low temperature were performed using a He closed-cycle cryostat. The lifetime measurements were acquired with the setup described for the luminescence spectra using a pulsed Xe−Hg lamp (6 μs pulse at half width and 20−30 μs tail). The absolute emission quantum yields were measured at room temperature using a Quantum Yield Measurement System C9920-02 from Hamamatsu with a 150 W xenon lamp coupled to a monochromator for wavelength discrimination, an integrating sphere as the sample chamber, and a multichannel analyzer for signal detection. The same amount of the powdered samples was grinded and pressed into pellets (1.5×10^8 N m^{2-}) with a 0.6 mm thickness.

The refractive index of Eu-AV-24 and mixed Eu,Gd-AV-24 were measured in an Abbe refractometer, A. Krüss Optronic, model AR3D, excitation wavelength of 590 nm.

Acknowledgment. We acknowledge the Portuguese Foundation for Science and Technology (FCT), PTDC and FEDER, EMMI for financial support of this work. We thank Prof. Sidney Ribeiro (UNESP Araraquara, Brazil) for useful discussions.

Supporting Information Available: Details on the crystal structure solution, refinement, and cif files of $K_7[Sm_3Si_{12}O_{32}]\cdot 3H_2O$ (Sm-AV-24) and $K_7[Eu_3Si_{12}O_{32}]\cdot 4H_2O$ (Eu-AV-24). Further analysis and structural drawings concerning the anionic $(Si_{12}O_{32})_n^{16n-}$ layers, Ln(1) and Ln(2) coordination environments, framework buildup, and crystal morphology. Details on the photoluminescence properties (emission, excitation and time-resolved spectra, $^5D_0$ lifetimes, and intensity parameters) of $K_7[Eu_3Si_{12}O_{32}]\cdot 4H_2O$ (Eu-AV-24) and $K_7[(Gd_{3-x}Eu_x)Si_{12}O_{32}]\cdot 4H_2O$ (Eu,Gd-AV-24). Dependence of the overlap integral on the Eu−Eu distance. This material is available free of charge via the Internet at http://pubs.acs.org.

JA901820Z